

This article appeared in a journal published by Elsevier. The attached copy is furnished to the author for internal non-commercial research and education use, including for instruction at the authors institution and sharing with colleagues.

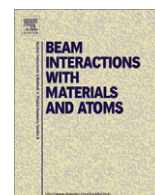
Other uses, including reproduction and distribution, or selling or licensing copies, or posting to personal, institutional or third party websites are prohibited.

In most cases authors are permitted to post their version of the article (e.g. in Word or Tex form) to their personal website or institutional repository. Authors requiring further information regarding Elsevier's archiving and manuscript policies are encouraged to visit:

<http://www.elsevier.com/copyright>

Contents lists available at [SciVerse ScienceDirect](http://www.sciencedirect.com)

## Nuclear Instruments and Methods in Physics Research B

journal homepage: [www.elsevier.com/locate/nimb](http://www.elsevier.com/locate/nimb)Nuclear reaction measurements of 95 MeV/u  $^{12}\text{C}$  interactions on PMMA for hadrontherapy

B. Braunn<sup>a</sup>, M. Labalme<sup>a,\*</sup>, G. Ban<sup>a</sup>, M. Chevallier<sup>c</sup>, J. Colin<sup>a</sup>, D. Cussol<sup>a</sup>, D. Dauvergne<sup>c</sup>, J.M. Fontbonne<sup>a</sup>, F. Haas<sup>b</sup>, A. Guertin<sup>e</sup>, D. Lebhertz<sup>b</sup>, F. Le Foulher<sup>c</sup>, C. Pautard<sup>a</sup>, C. Ray<sup>c</sup>, M. Rousseau<sup>b</sup>, M.D. Salsac<sup>d</sup>, L. Stuttge<sup>b</sup>, E. Testa<sup>c</sup>, M. Testa<sup>c</sup>

<sup>a</sup> LPC Caen, ENSICAEN, Université de Caen, CNRS/IN2P3, Caen, France<sup>b</sup> IPHC Strasbourg, France<sup>c</sup> IPN Lyon, France<sup>d</sup> CEA/IRFU/SPhN Saclay, France<sup>e</sup> SUBATECH, CNRS/IN2P3, École des Mines et Université de Nantes, Nantes, France

## ARTICLE INFO

## Article history:

Received 30 May 2011

Received in revised form 3 August 2011

Available online 23 August 2011

## Keywords:

Hadrontherapy

 $^{12}\text{C}$  fragmentation

## ABSTRACT

The ion dose deposition in tissues is characterized by a favorable depth dose profile (i.e. Bragg peak) and a small lateral spread. In order to keep these benefits of ions in cancer treatments, a very high accuracy is required on the dose deposition ( $\pm 3\%$ ). For given target stoichiometry and geometry, the largest uncertainty on the physical dose deposition is due to the ion nuclear fragmentation. We have performed an experiment at GANIL with a 95 MeV/u  $^{12}\text{C}$  beam on thick tissue equivalent PMMA targets (thicknesses: 5, 10, 15, 20 and 25 mm). The main goals of this experiment are to provide experimental fragmentation data for benchmarking the physical models used for treatment planning. Production rates, energy and angular distributions of charged fragments have been measured. The purpose of this paper is to present the results of this experiment.

© 2011 Elsevier B.V. All rights reserved.

## 1. Introduction

Carbon ions with energy ranging from 80 to 400 MeV/u are used in hadrontherapy to treat cancerous tumors. Compared to conventional radiotherapy, it presents two main advantages: a precise ballistic, with a finite range and a maximum dose deposition at the end of the path of the ions (i.e. Bragg peak) and an enhanced biological efficiency in the Bragg peak region.

To keep these benefits, the treatments require a very high accuracy on the physical dose deposition. The energy deposited in the target volume has to be determined with an accuracy of 3% and its location has to be determined with an accuracy of  $\sim 1$  mm. The largest uncertainty on the physical dose deposition relies on the ion fragmentation process along its penetration path in the patient tissues ([1]). This process leads to an attenuation of the primary beam flux and to an increase of the number of lower Z fragments with the increasing penetration depth. The fragments contribute to the deposited dose in the Bragg-peak and must be taken into account for the evaluation of the biological effects [2]. They also contribute to spread the dose longitudinally and

transversally in the surrounding healthy tissues. This is especially the case for hydrogen and helium isotopes which have a longer path and a larger angular scattering than carbon ions.

Simulation codes are used to compute the transport of ions in matter. They include deterministic codes: TRiP (developed at GSI [3]) or HIBRAC ([4]), and Monte Carlo codes: SHIELD-HIT, FLUKA, GEANT4, PHITS... ([5–7]). Uncertainties on the dose calculations are dominated by the uncertainties on fragmentation cross sections and on nuclear reaction models. Thus nuclear cross sections are critical inputs for these simulation frameworks. In particular there is a lack of experimental cross section data available for light ions on light targets in the energy range 30–200 MeV/u. Most of the data used by the simulation frameworks are empirically extrapolated from the experimental values measured at higher energies.

To improve the knowledge on the  $^{12}\text{C}$  fragmentation process, experiments have been performed in Japan and in Europe for more than 15 years. Measurements of light charged fragment production in water and PMMA have been started by the Japanese treatment centers (Chiba and Hyogo). They have performed complete measurements of carbon ions fragmentation in PMMA phantoms in the energy range 200–400 MeV/u ([8–10]). Similar experiments have also been performed by the GSI biophysics department. Light

\* Corresponding author. Tel.: +33 2 31 45 25 17; fax: +33 2 31 45 25 49.

E-mail address: [labalme@lpccaen.in2p3.fr](mailto:labalme@lpccaen.in2p3.fr) (M. Labalme).

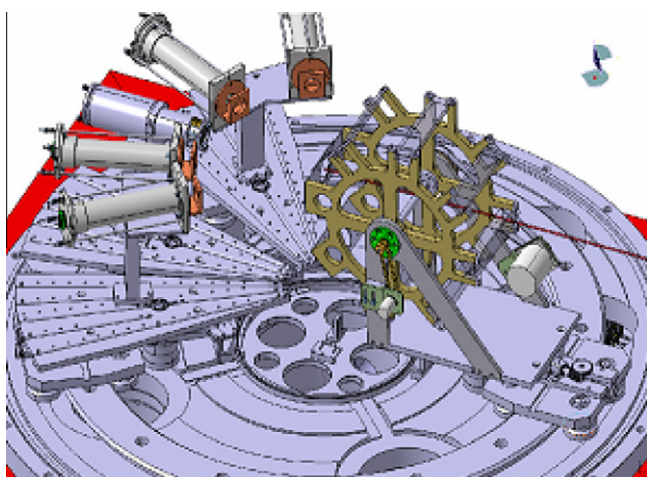


Fig. 1. Schematic view of the experimental set up.

charged ions and neutron production rates due to the fragmentation of a carbon projectile in water have been measured for beam energies ranging from 200 to 400 MeV/u ([11–13]). All these measurements allowed the determination of the integrated flux and the energy distributions of the fragments relative to the water depth. These data have been implemented in treatment planning systems (TPS) like TRiP. They can also be used to constrain nuclear reaction models ([14]). Nevertheless, it is difficult to constrain the nuclear reaction models by a direct comparison with thick targets experiments then, in order to directly constrain nuclear reaction models, we will perform a second experiment at 95 MeV/u at GANIL in 2011 with thin targets.

To extend these data to the lowest part of the energy range of hadrontherapy, an experiment with a 95 MeV/u  $^{12}\text{C}$  beam on PMMA tissue equivalent targets has been performed by our collaboration in May 2008 at GANIL. The experimental set-up will be presented in the next section. The obtained results will be presented in the Section 4. Then, an estimation of the dose in the thin silicon detector will be shown.

## 2. Experimental set-up

The experiment has been performed with the ECLAN reaction chamber at the GANIL G22 beam line. A schematic view of the experimental set-up is shown on Fig. 1. It included five three-layer  $\Delta E/\Delta E/E$  telescopes for charged particles detection. These telescopes are located inside the reaction chamber, 22 cm behind the backward side of the targets. The telescopes are fixed on the rotating arms of the ECLAN chamber. This allows covering angles ranging from  $7^\circ$  to  $70^\circ$  for the thinnest targets and from  $0^\circ$  to  $70^\circ$  for

targets thicker than 20 mm, since the range of 95 MeV/u  $^{12}\text{C}$  in PMMA is 20 mm. The targets are set on a rotating wheel in the center of the reaction chamber. The wheel supports six PMMA ( $\text{C}_5\text{H}_8\text{O}_2$ ;  $d = 1.19 \text{ g/cm}^3$ ) targets of different thicknesses: 5, 10, 15, 20, 25 and 40 mm and an empty slot. These various target thicknesses allow to measure fragment production rates all along the carbon path up to the Bragg peak and beyond.

The five  $\Delta E_{\text{thin}}/\Delta E_{\text{thick}}/E$  detectors are composed of two Si detectors followed by a scintillator. The silicon detectors are 80 and 500  $\mu\text{m}$  thick. The last stage of four telescopes consists in a 7.5 cm long CsI scintillator. For one of the telescopes the last stage consists in a 7.6 cm long BGO. This last telescope has been used for the lowest angles from  $0^\circ$  to  $20^\circ$  in order to detect protons up to 200 MeV. The characteristics of these detectors are given in Table 1.

The measurement is triggered when the second stage of a telescope is hit. Thus, the acceptance of the telescopes is calculated using the distance  $d$  between the second Si stage and the backward side of the target. For the “BGO” telescope, the surface  $S$  of the active part of the telescope corresponds to the silicon surface. For the “CsI” telescope, the surface used to compute the acceptance is the intersection between a mechanical support (Thickness: 1.1 cm,  $\varnothing$ : 2 cm) located between the scintillator and the second Si stage, and the rectangular surface of the Si.

The beam monitor is a critical tool for accurate cross section measurements. In this experiment, it is based on the measurement of fluorescence X-rays emitted by a thin Ag foil (7  $\mu\text{m}$  thick) set in the beam in front of the reaction chamber. X-rays are detected by means of two detectors (Si(Li) and Ge) located at  $90^\circ$  with respect to the beam direction. These two detectors are calibrated at low beam intensity ( $<10^5$  ions/s) by means of a plastic scintillator intercepting the beam. This monitor is particularly well suited in the  $10^4$ – $10^8$  ions/s intensity range and has given an accuracy of  $\sim 5\%$  on the whole intensity range of the experiment.

## 3. Data analysis

### 3.1. Particle identification

The energy loss of charged particles in matter depends on their charge and mass. The  $\Delta E/E$  technique uses this property for the identification of the charged particles. Fig. 2 shows examples of identification maps, at  $40^\circ$  and for the 15 mm thick PMMA target. The hyperboles correspond to protons, deuterons, tritons, helium3 and alphas. The left-hand side of Fig. 2 represents the energy measured in the thin Si detector relative to the energy measured in the thick silicon detector. The hyperboles back bending corresponds to the particles which “punch through” the second stage of the telescope. The right-hand side shows the energy measured in the thick Si detector relative to the energy measured in the CsI scintillator. It allows identifying the particles that punch through the two Si stages. The black lines represent the identification contours used

Table 1  
Characteristics of the charged particle telescopes.

	1st stage	2nd stage	3rd stage	Acceptance
TEL1-2-3-4	Si Hexahedron Thickness: 89 $\mu\text{m}$ L: 1.5 cm, H: 2 cm	Si Hexahedron Thickness: 507 $\mu\text{m}$ L: 1.5 cm, H: 2 cm	CsI Cylinder Length: 7.5 cm $\varnothing$ : 3 cm	S: 2.69 $\text{cm}^2$ d: 22.2 cm 5.45 msr
TELBGO	Si Cylinder Thickness: 80 $\mu\text{m}$ $\varnothing$ : 1.954 cm	Si Cylinder Thickness: 519 $\mu\text{m}$ $\varnothing$ : 1.954 cm	BGO Cylinder Length: 7.62 cm $\varnothing$ : 2.54 cm	S: 2.99 $\text{cm}^2$ d: 22.3 cm 6 msr



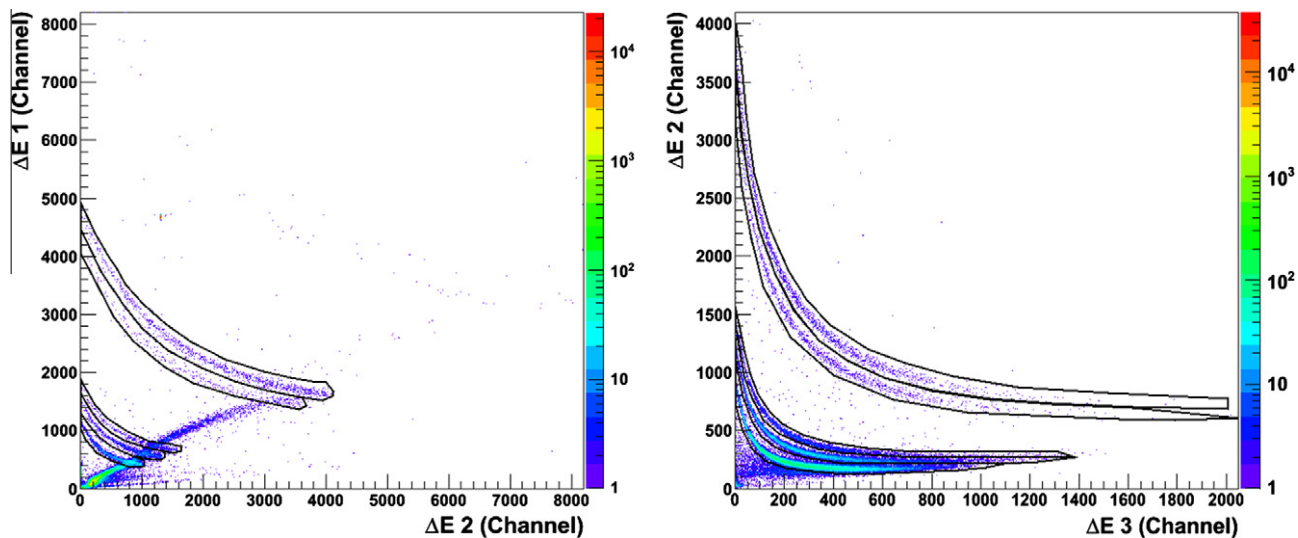


**Fig. 2.** Left-hand side: identification matrix between the first stage and the second stage of a telescope. The black lines correspond to the selection applied for proton, deuteron, triton, helium 3 and alpha particles. Right-hand side: identification matrix between the second stage and the third stage of a telescope (CsI).

**Table 2**

Energy thresholds as a function of the charge of the detected particles.

Nuclear charge	Threshold (MeV)
1	2
2	10
3	18
4	28
5	42
6	60

to select the particles in charge and mass. A good mass discrimination has been obtained from hydrogen to carbon isotopes for the four telescopes with a CsI scintillator. Due to the poor energy resolution of the BGO scintillator, only charge discrimination has been obtained with the “BGO” telescope.

The identification threshold is driven by the thickness of the first stage of the telescope. To be identified, a particle has to pass through the first thin Si stage and has to deposit energy in the

second stage. This leads to an energy threshold that corresponds to the minimum energy necessary to pass through the 80  $\mu\text{m}$  thick Si stage. The threshold values for the different particles are summarized in Table 1. Because of the thickness of the last telescope stage, protons with energy greater than 160 MeV for the CsI and greater than 200 MeV for the BGO pass through the scintillator. Hence only protons having energy lower than 160 MeV for the CsI and lower than 200 MeV for the BGO have been identified (Table 2).

### 3.2. Energy calibration

The energy calibration of the two Si stages has been performed by using the “punch through energy” that can be accurately calculated knowing the thicknesses of the silicon detectors. For each isotope, the energy deposited in the two Si stages that corresponds to the “punch through energy” is computed by using SRIM ([15]) simulations and associated to the corresponding channel value. The left-hand side of Fig. 3 shows an example of the calibration points obtained for the thick Si of one telescope thanks to this method.

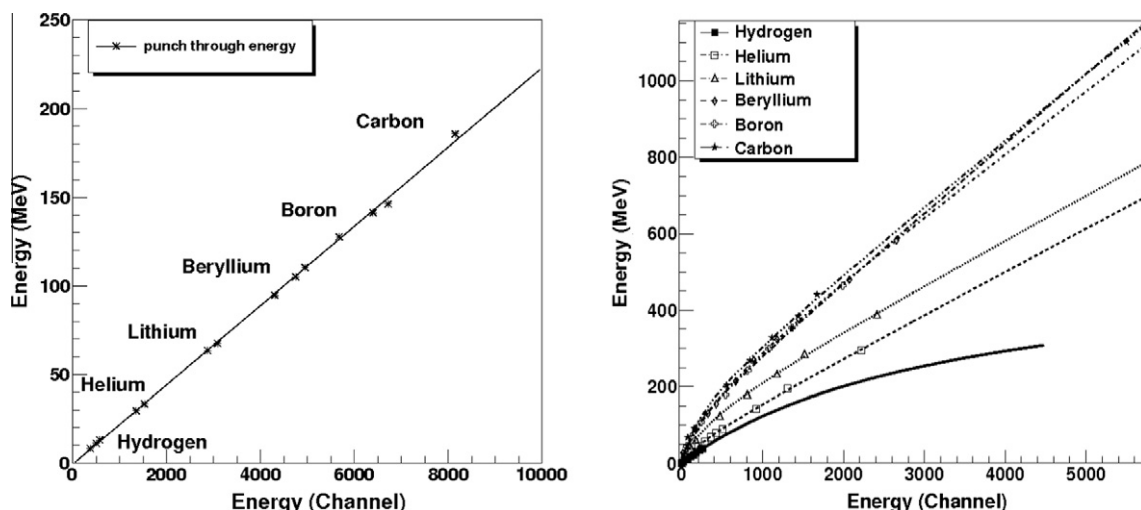


**Fig. 3.** Left-hand side: energy calibration points for the second stage of a telescope. The black line corresponds to a linear fit. Right-hand side: calibration points for the third stage of a telescope (BGO scintillator). The lines correspond to fits using the calibration function given by Eq. (1).

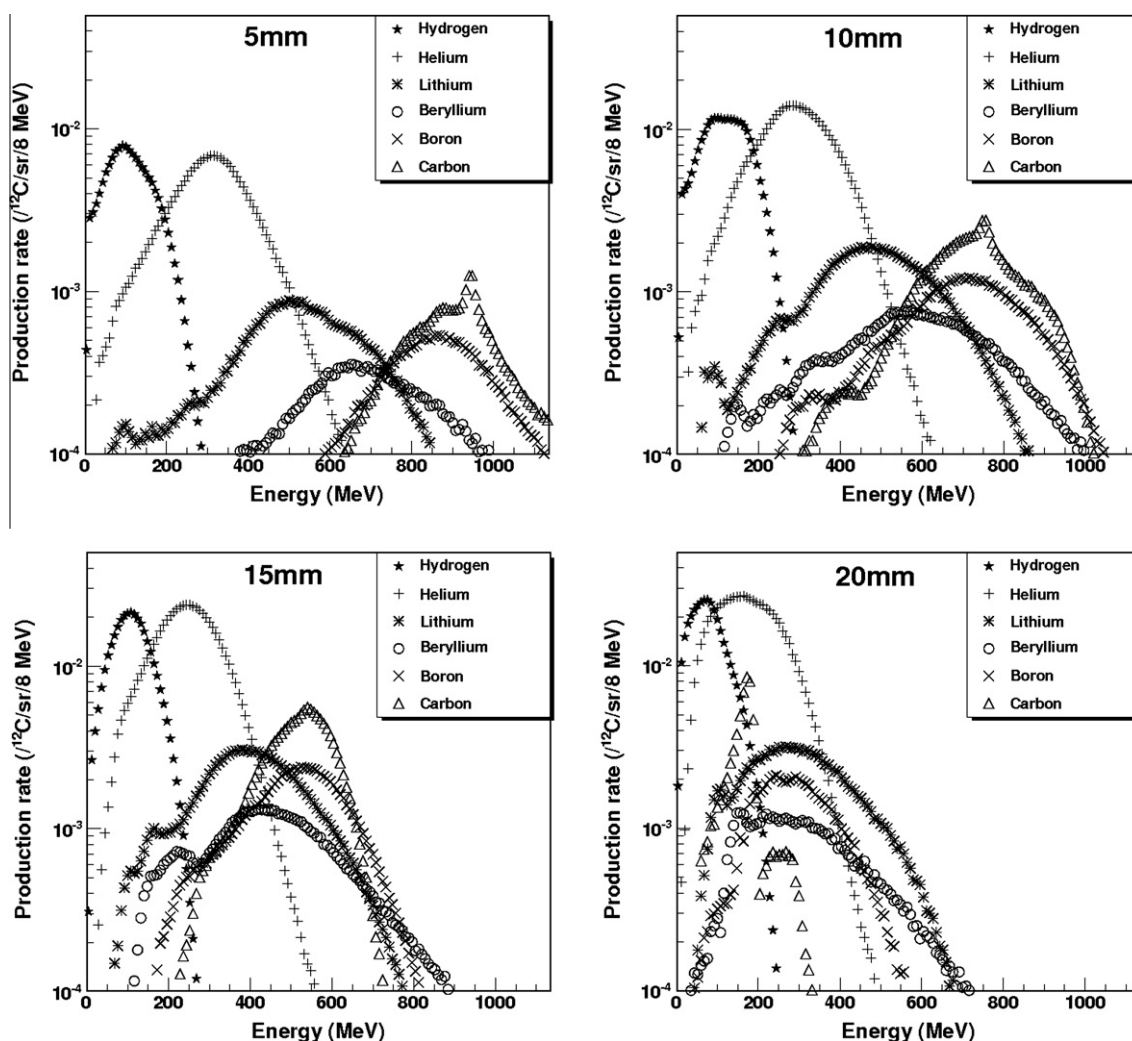


**Fig. 4.** Energy spectra in MeV for charged fragments emitted at 7° for the 5 mm (upper left panel), 10 mm (upper right panel), 15 mm (lower left panel) and 20 mm (lower right panel) thick PMMA targets.

The linear correlation between the channel number and the energy does not depend on the fragment type. A linear fit has been performed on each Si detector in order to obtain the calibration parameters.

The energy calibration of the scintillator is slightly more complicated since the creation of light resulting from the energy deposition in the scintillators depends on the nature of the particle. Then a specific calibration function has to be determined for each isotope. The SRIM simulations allow to determine the energy deposited in the scintillator from the energy deposited in the thick silicon detector. The correspondence between the channel number and the energy deposited in the scintillator has been obtained for each isotope. An example of this energy calibration is shown on the right-hand side of Fig. 3 for Z = 1 and 2 isotopes.

The following formula has been used to extract the energy from the channel values:

$$E_{\text{MeV}} = \frac{a_0 \cdot E_{\text{channel}}}{1 + a_1 \cdot E_{\text{channel}}} + a_2 + a_3 \cdot E_{\text{channel}}, \quad (1)$$

Eq. (1) takes into account the quenching at small energy and the linear response of the scintillator at high energy. The four free parameters  $a_0$ ,  $a_1$ ,  $a_2$  and  $a_3$  have been determined for each scintillator and for each isotope. Lines on the right-hand side of Fig. 3 represent an example of the calibration functions obtained with Eq. (1). Due to the small values of the “punch through energies”,

the calibration parameters are not constrained for the high energies. As a consequence, the accuracy of this energy calibration is lower at high energies.

## 4. Results

### 4.1. Energy distributions

Thanks to the particle identifications and energy calibrations, the energy distributions of charged particles have been obtained for the six PMMA targets at seven angles. The energy distributions of the charged fragments obtained at 7° with PMMA thickness from 5 to 20 mm are illustrated on Fig. 4.

These spectra exhibit the large range of the fragments energy. The Z = 1 ions reach very high energies, greater than 200 MeV. The energy of the fragments decreases with the thickness of the target due to the energy loss of the particles along their path in matter.

For the 5 mm thick target (upper left panel), the Z = 6 most probable energy (~950 MeV, i.e. 80 MeV/u) is close to the expected energy of the  $^{12}\text{C}$  beam taking into account the energy loss in the target. For lighter fragments, the most probable energy per nucleon is very close to 80 MeV/u (~90 MeV for Z = 1, 350 MeV for Z = 2, ~500 MeV for Z = 3, ~650 MeV for Z = 4 and ~850 MeV for Z = 5).

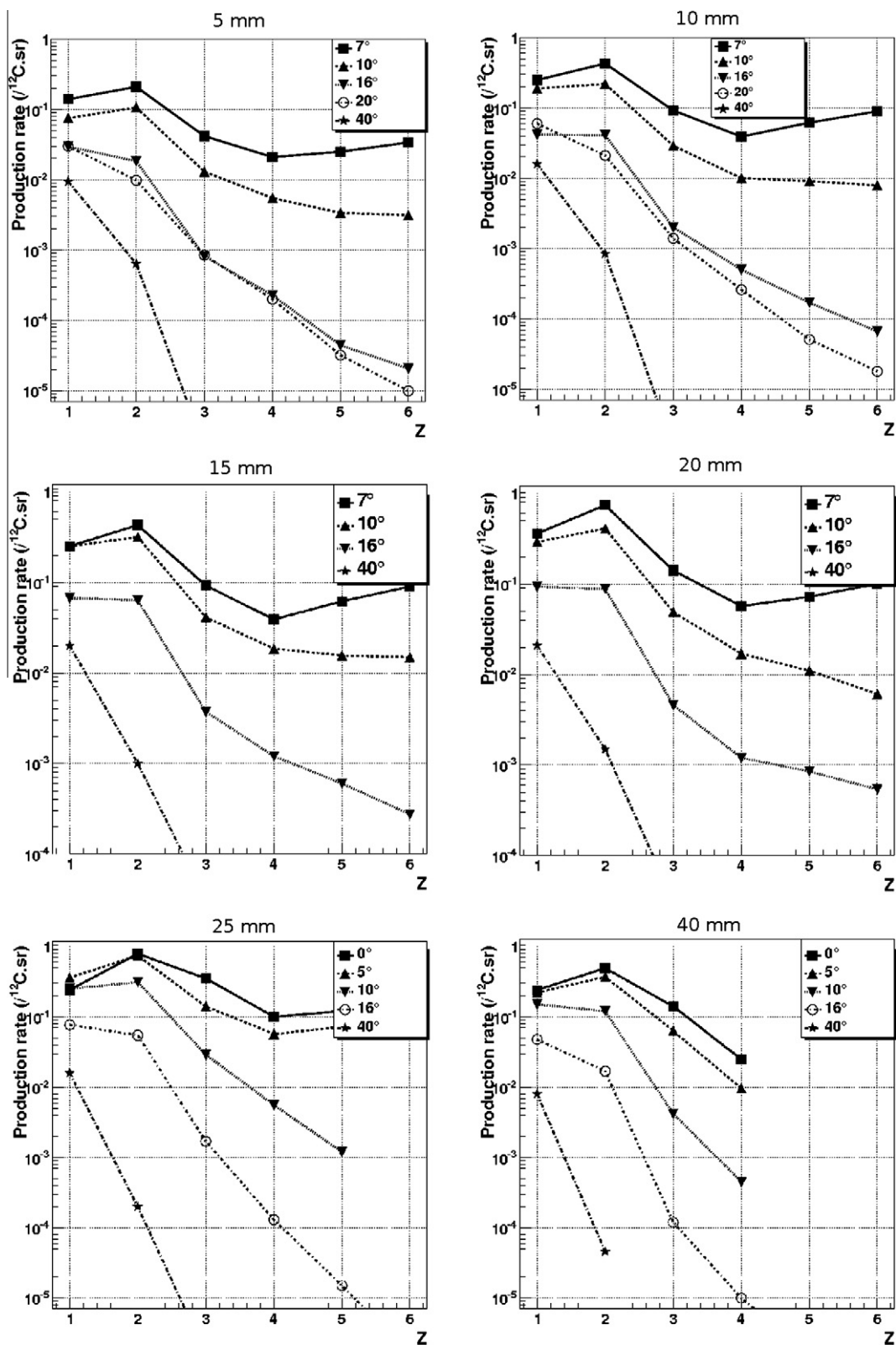


Fig. 5. Z = 1–6 fragment production rates for the six different PMMA thicknesses: 5, 10, 15, 20, 25 and 40 mm.

This trend is also observed for the thicker targets up to the thickness corresponding to the  $^{12}\text{C}$  range in the PMMA (20 mm). The most probable energy for all fragments is decreasing with the PMMA target thickness, as expected. This strongly indicates that the detected fragments are produced by the fragmenting pro-

jectile. These observations are compatible with results of [16]. Most of the fragments issued from the target nuclei have low energies and hence are stopped in the PMMA thick target. The lower part of the energy distributions are probably due to target nuclei fragments produced at the backward edge of the PMMA target.

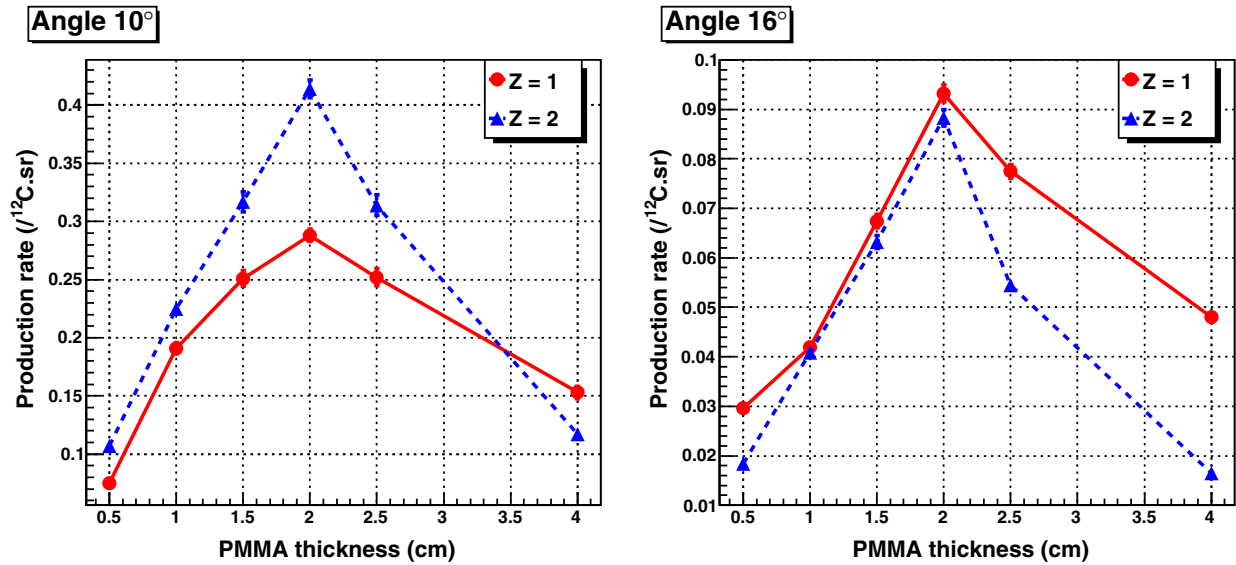


Fig. 6. Production rate evolution as a function of PMMA thickness at 10° (left) and 16° (right) for Z = 1 and Z = 2 fragments.

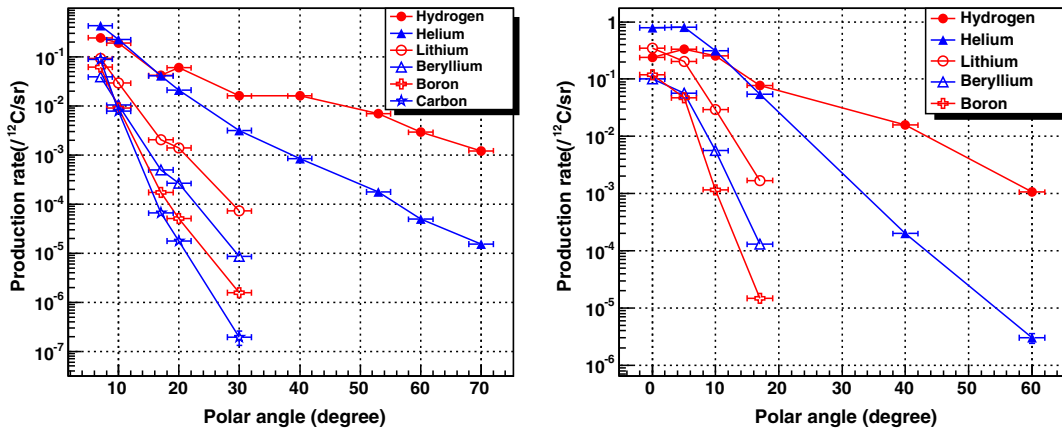


Fig. 7. Angular distributions of the charged fragments production for 10 mm (left) and 25 mm (right) thick PMMA targets (statistical errors and angular uncertainties are represented in this figure).

#### 4.2. Production rates

Production rates of Z = 1–6 fragments for the six PMMA targets have been obtained by integrating the number of particles in the identification contours (Cf. Fig. 2). All the production rates with the corresponding statistical errors are given in the tables in the Appendix A. Due to the acceptance of the telescopes, and to the mechanical accuracy of the rotating arms of the reaction chamber, angle measurements are given with an uncertainty of  $\pm 2^\circ$ .

Fig. 5 shows the production rates of Z = 1–6 for the six different PMMA thicknesses. Since the systematic errors are difficult to determine, only statistical errors (lower than 5%) are presented on this figure and are included in the symbol sizes. Systematic errors have been estimated to be around 10–20% for all the particles with a charge greater than or equal to 2 and mainly include uncertainties on the choice of identification contours in the DE/E spectra. These errors have been determined by comparing the production rates obtained for different runs for the same telescope angles. For particles with Z = 1, the production rates measured with the CsI telescopes are probably underestimated since the particles with an energy greater than 120 MeV can escape out of the scintil-

lator. This underestimation is significant only at small angles (9° and 16°).

Experimental production rates exhibit the predominance of the production of Z = 1 and 2 fragments. Similar results at 7° with a 270 MeV/u <sup>12</sup>C beam in water have been obtained by Golovkov et al. in [17]. It should be noticed that Z = 2 are predominant at forward angles ( $\leq 10^\circ$ ). This is consistent with a 3 $\alpha$  cluster structure of <sup>12</sup>C as expressed in [18]. This comportment has also been observed at GSI with higher energies incident <sup>12</sup>C in water targets as shown in [21,22]. The productions of Z = 5 and 6 fragments are not measured for thicknesses above 20 mm. This value corresponds to the range of <sup>12</sup>C at 95 MeV/u in PMMA. The production rates for Z  $\geq 3$  fragments are not measurable at angles greater than 30° (limited statistics).

Fig. 6 shows the evolution of production rates with respect to target thickness for charges 1 and 2 at 10° and 16°. This evolution results from the balance between the amount of <sup>12</sup>C fragmentation which produces fragments and the fragment paths in PMMA targets. The increase of the fragment production from 5 to 20 mm is due to the increase of <sup>12</sup>C fragmentation with target thickness. The decrease of the production rates for PMMA targets thicker than



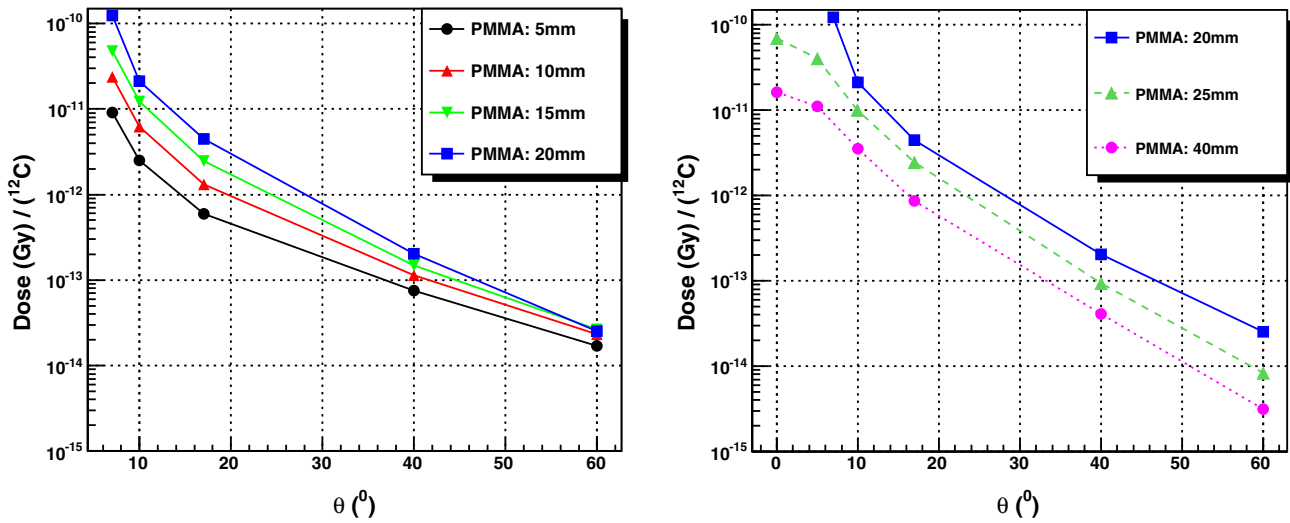


Fig. 8. Dose in the first Si detector for different PMMA thicknesses.

20 mm is due to the absorption of the fragments after the Bragg peak depth.

#### 4.3. Angular distributions

An example of angular distributions for  $Z = 1$ –6 fragments for the 10 and 25 mm thick PMMA targets is shown on Fig. 7. These production rates have been obtained with statistical errors better than 5%.

As already shown, Fig. 7 shows the predominance of  $Z = 1$  and 2. Fig. 7 also exhibits that the angular distributions are most forward peaked for the heaviest fragments, as expected. Around  $10^\circ$ , a crossing between  $Z = 1$  and 2 angular distributions is noticed and helium becomes the most abundant particle at forward angles. This inversion has also been observed by Gunzert-Marx et al. and Matsufuji et al. in experiments with 200 MeV/u ([13]) and 290 MeV/u ([9])  $^{12}\text{C}$  beams in thick water targets. The angular spreading is important for the light fragments ( $Z = 1$  and 2) which are detected up to  $70^\circ$ . This is particularly true for  $Z = 1$  for which there is only a decrease by two orders of magnitude between  $10^\circ$  and  $70^\circ$  for the thinnest targets.

These results confirm that the lightest fragments ( $Z = 1$  and 2) mainly contribute to the scatter of the dose far from the original beam direction due to their large angular deflection. Heavier fragments that are emitted with small angles will essentially contribute to the dose deposition in and close to the target volume.

#### 4.4. Dose estimation

An estimation of the dose in the thin silicon detector for the different targets can be performed by integrating the energy deposited in the thin Si detector ( $\sim 80 \mu\text{m}$  thick, surface:  $300 \text{ mm}^2$ ). The estimation of the dose is obtained by dividing the energy deposited in the Si detector by the mass of silicon of the detector as given in Eq. (2), where  $\rho \cdot S \cdot e$  is the mass of Silicon (where  $\rho$  is the Si density in  $\text{g/cm}^3$ ,  $S$  the surface of the silicon diode in  $\text{cm}^2$  and  $e$  its depth in cm) and  $N(\Delta E) \times \Delta E$  the deposited energy in MeV (where  $N(\Delta E)$  is the number of fragments that deposited an energy  $\Delta E$  in the silicon detector during the run). This dose is then normalized relative to the number of incident  $^{12}\text{C}$ .

$$D_{\text{tot}} = \sum_{\Delta E} \left[ 1,6 \cdot 10^{-10} \times \Delta E \times N(\Delta E) \times \frac{1}{\rho \cdot S \cdot e} \right], \quad (2)$$

This leads to an estimation of the dose deposited per incident  $^{12}\text{C}$  at different angles in  $80 \mu\text{m}$  of Si for a given PMMA thickness. The results are shown on Fig. 8.

The dose increases with the PMMA target thickness up to 20 mm (left-hand side panel) and decreases beyond this range (right-hand side panel). This is mainly due to the number of secondary fragments which exhibits the same behavior as shown in Fig. 5. It should also be noticed that the dose decreases drastically with the distance to the beam axis and the dose per incident  $^{12}\text{C}$  becomes rapidly small.

#### 5. Conclusion

A first experiment has been achieved at GANIL with a 95 MeV/u  $^{12}\text{C}$  beam on thick PMMA targets. Six different target thicknesses ranging from 5 to 40 mm have been used to study the fragment production. The production rates, angular distributions and energy spectra have been measured for charged particles (protons to carbon ions) at seven angles ( $0$ – $70^\circ$ ). The mean energy of the fragments corresponds to the energy per nucleon of the beam, indicating that most of the fragments are emitted by the projectile during the nuclear reaction. The production rates exhibit the predominance of light particles production ( $Z < 3$ ). The production of  $Z = 2$  is even the most important at forward angles. These observations are compatible with existing data at higher energies. These data at  $\sim 100 \text{ MeV/u}$  will complete the fragmentation production data for the lowest energies used in hadrontherapy. The  $Z = 1$  and 2 fragments are the main contributors to the dose delocalization (high rates, high energies, high angular dispersions) whereas heavier fragments contribute to the dose in and close to the tumor.

Since fragments are produced by projectiles at different energies in the thick targets, it is difficult to constraint the nuclear reaction models by a direct comparison between the results of these models and the presented experimental results. This is especially true if different models are necessary for different energy ranges. In that case, complex Monte-Carlo simulation environments such as GEANT4 [19] or FLUKA [20] are necessary.

Then, in the continuing effort to obtain the required physical data for hadrontherapy and in order to directly constraint nuclear reaction models, a second experiment at GANIL has been performed in May 2011, focusing on double cross section measurements on thin target for C–C, C–O, C–H and C–Ca reactions at 95 MeV/u.



Table 1. Production rates with statistical error in function of the charge of the fragments and the angle of detection for the 0.5 cm PMMA target. Values are in counts/(incident  $^{12}\text{C.sr}$ ).

PMMA thickness: 0.5 cm						
Angle	Nuclear charge					
	Z1	Z2	Z3	Z4	Z5	Z6
7°-BGO	$1.4\text{E}-0 \pm 4\text{E}-03$	$2.1\text{E}-01 \pm 6\text{E}-03$	$4.2\text{E}-02 \pm 1\text{E}-03$	$2.1\text{E}-02 \pm 7\text{E}-04$	$2.5\text{E}-02 \pm 8\text{E}-04$	$3.4\text{E}-02 \pm 1\text{E}-03$
10°-BGO	$7.5\text{E}-02 \pm 2\text{E}-03$	$1.1\text{E}-01 \pm 3\text{E}-03$	$1.3\text{E}-02 \pm 3\text{E}-04$	$5.5\text{E}-03 \pm 1\text{E}-04$	$3.4\text{E}-03 \pm 9\text{E}-05$	$3.1\text{E}-03 \pm 9\text{E}-05$
16°	$3.0\text{E}-02 \pm 6\text{E}-04$	$1.8\text{E}-02 \pm 4\text{E}-04$	$8.1\text{E}-04 \pm 2\text{E}-05$	$2.3\text{E}-04 \pm 8\text{E}-06$	$4.4\text{E}-05 \pm 2\text{E}-06$	$2.1\text{E}-05 \pm 1\text{E}-06$
20°-BGO	$3.0\text{E}-02 \pm 7\text{E}-04$	$9.8\text{E}-03 \pm 2\text{E}-04$	$8.5\text{E}-04 \pm 2\text{E}-05$	$2.0\text{E}-04 \pm 6\text{E}-06$	$3.2\text{E}-05 \pm 1\text{E}-06$	$1.0\text{E}-05 \pm 6\text{E}-07$
30°	$8.4\text{E}-03 \pm 2\text{E}-04$	$1.8\text{E}-03 \pm 5\text{E}-05$	$4.6\text{E}-05 \pm 2\text{E}-06$	$8.2\text{E}-06 \pm 5\text{E}-07$	$1.1\text{E}-06 \pm 1\text{E}-07$	$1.3\text{E}-07 \pm 4\text{E}-08$
40°	$9.4\text{E}-03 \pm 2\text{E}-04$	$6.4\text{E}-04 \pm 2\text{E}-05$				
53°	$4.5\text{E}-03 \pm 1\text{E}-04$	$1.6\text{E}-04 \pm 5\text{E}-06$				
60°	$2.1\text{E}-03 \pm 5\text{E}-05$	$4.7\text{E}-05 \pm 3\text{E}-06$				
70°	$1.0\text{E}-03 \pm 3\text{E}-05$	$1.5\text{E}-05 \pm 8\text{E}-07$				

Table 2. Production rates with statistical error in function of the charge of the fragments and the angle of detection for the 1 cm PMMA target. Values are in counts/(incident  $^{12}\text{C.sr}$ ).

PMMA thickness: 1 cm						
Angle	Nuclear charge					
	Z1	Z2	Z3	Z4	Z5	Z6
7°-BGO	$2.5\text{E}-01 \pm 7\text{E}-03$	$4.3\text{E}-01 \pm 3\text{E}-04$	$9.2\text{E}-02 \pm 3\text{E}-03$	$3.9\text{E}-02 \pm 1\text{E}-03$	$6.2\text{E}-02 \pm 2\text{E}-03$	$9.0\text{E}-02 \pm 3\text{E}-03$
10°-BGO	$1.9\text{E}-01 \pm 5\text{E}-03$	$2.2\text{E}-01 \pm 1\text{E}-04$	$2.9\text{E}-02 \pm 8\text{E}-04$	$1.0\text{E}-02 \pm 3\text{E}-04$	$9.1\text{E}-03 \pm 2\text{E}-04$	$7.9\text{E}-03 \pm 2\text{E}-04$
16°	$4.2\text{E}-02 \pm 9\text{E}-04$	$4.1\text{E}-02 \pm 5\text{E}-05$	$2.0\text{E}-03 \pm 5\text{E}-05$	$5.0\text{E}-04 \pm 2\text{E}-05$	$1.7\text{E}-04 \pm 6\text{E}-06$	$6.6\text{E}-05 \pm 3\text{E}-06$
20°-BGO	$6.0\text{E}-02 \pm 1\text{E}-03$	$2.1\text{E}-02 \pm 2\text{E}-05$	$1.4\text{E}-03 \pm 4\text{E}-05$	$2.6\text{E}-04 \pm 8\text{E}-06$	$5.1\text{E}-05 \pm 2\text{E}-06$	$1.8\text{E}-05 \pm 9\text{E}-07$
30°	$1.6\text{E}-02 \pm 4\text{E}-04$	$3.2\text{E}-03 \pm 7\text{E}-06$	$7.2\text{E}-05 \pm 3\text{E}-06$	$8.5\text{E}-06 \pm 5\text{E}-07$	$1.6\text{E}-06 \pm 2\text{E}-07$	$1.9\text{E}-07 \pm 6\text{E}-08$
40°	$1.6\text{E}-02 \pm 3\text{E}-04$	$8.5\text{E}-04 \pm 7\text{E}-06$				
53°	$7.0\text{E}-03 \pm 2\text{E}-04$	$1.8\text{E}-04 \pm 2\text{E}-06$				
60°	$2.9\text{E}-03 \pm 7\text{E}-05$	$4.9\text{E}-05 \pm 2\text{E}-06$				
70°	$1.2\text{E}-03 \pm 2\text{E}-05$	$3\text{E}-05 \pm 5\text{E}-07$				

Table 3. Production rates with statistical error in function of the charge of the fragments and the angle of detection for the 1.5 cm PMMA target. Values are in counts/(incident  $^{12}\text{C.sr}$ ).

PMMA thickness: 1.5 cm						
Angle	Nuclear charge					
	Z1	Z2	Z3	Z4	Z5	Z6
7°-BGO	$3.4\text{E}-01 \pm 9\text{E}-03$	$6.4\text{E}-01 \pm 2\text{E}-02$	$1.3\text{E}-01 \pm 4\text{E}-03$	$7.2\text{E}-02 \pm 2\text{E}-03$	$9.6\text{E}-02 \pm 3\text{E}-03$	$1.5\text{E}-01 \pm 4\text{E}-03$
10°-BGO	$2.5\text{E}-01 \pm 7\text{E}-03$	$3.2\text{E}-01 \pm 9\text{E}-03$	$4.1\text{E}-02 \pm 1\text{E}-03$	$1.9\text{E}-02 \pm 6\text{E}-04$	$1.6\text{E}-02 \pm 5\text{E}-04$	$1.5\text{E}-02 \pm 4\text{E}-04$
16°	$6.7\text{E}-02 \pm 1\text{E}-03$	$6.3\text{E}-02 \pm 1\text{E}-03$	$3.7\text{E}-03 \pm 9\text{E}-05$	$1.2\text{E}-03 \pm 3\text{E}-05$	$6.0\text{E}-04 \pm 2\text{E}-05$	$2.8\text{E}-04 \pm 1\text{E}-05$
40°	$2.0\text{E}-02 \pm 4\text{E}-04$	$1.0\text{E}-03 \pm 3\text{E}-05$				
60°	$3.0\text{E}-03 \pm 7\text{E}-05$	$5.4\text{E}-05 \pm 3\text{E}-06$				

Table 4. Production rates with statistical error in function of the charge of the fragments and the angle of detection for the 2 cm PMMA target. Values are in counts/(incident  $^{12}\text{C.sr}$ ).

PMMA thickness: 2 cm						
Angle	Nuclear charge					
	Z1	Z2	Z3	Z4	Z5	Z6
7°-BGO	$3.6\text{E}-01 \pm 1\text{E}-02$	$7.4\text{E}-01 \pm 2\text{E}-02$	$1.4\text{E}-01 \pm 4\text{E}-03$	$5.7\text{E}-02 \pm 2\text{E}-03$	$7.2\text{E}-02 \pm 2\text{E}-03$	$1.0\text{E}-01 \pm 4\text{E}-03$
9°	$2.1\text{E}-01 \pm 7\text{E}-03$	$4.6\text{E}-01 \pm 2\text{E}-02$	$4.4\text{E}-02 \pm 2\text{E}-03$	$2.0\text{E}-02 \pm 7\text{E}-04$	$1.9\text{E}-02 \pm 7\text{E}-04$	$1.3\text{E}-02 \pm 5\text{E}-04$
10°-BGO	$2.9\text{E}-01 \pm 5\text{E}-03$	$4.1\text{E}-01 \pm 7\text{E}-03$	$4.9\text{E}-02 \pm 9\text{E}-04$	$1.7\text{E}-02 \pm 3\text{E}-04$	$1.1\text{E}-02 \pm 3\text{E}-04$	$6.1\text{E}-03 \pm 1\text{E}-04$
16°	$9.3\text{E}-02 \pm 2\text{E}-03$	$8.8\text{E}-02 \pm 2\text{E}-03$	$4.6\text{E}-03 \pm 1\text{E}-04$	$1.2\text{E}-03 \pm 3\text{E}-05$	$8.5\text{E}-04 \pm 3\text{E}-05$	$5.4\text{E}-04 \pm 2\text{E}-05$
33°	$4.0\text{E}-02 \pm 1\text{E}-03$	$5.1\text{E}-03 \pm 2\text{E}-04$				
40°	$2.1\text{E}-02 \pm 4\text{E}-04$	$1.5\text{E}-03 \pm 4\text{E}-05$				
60°	$2.4\text{E}-03 \pm 5\text{E}-05$	$5.2\text{E}-05 \pm 3\text{E}-06$				

Table 5. Production rates with statistical error in function of the charge of the fragments and the angle of detection for the 2.5 cm PMMA target. Values are in counts/(incident  $^{12}\text{C.sr}$ ).

PMMA thickness: 2.5 cm						
Angle	Nuclear charge					
	Z1	Z2	Z3	Z4	Z5	Z6
0°-BGO	2,4E–01 ± 7E–03	7,9E–01 ± 2E–02	3,5E–01 ± 1E–02	1,0E–01 ± 3E–03	1,2E–01 ± 4E–03	
5°-BGO	3,4E–01 ± 9E–03	8,0E–01 ± 2E–02	2,0E–01 ± 5E–03	5,7E–02 ± 2E–03	4,7E–02 ± 1E–03	
10°-BGO	2,5E–01 ± 7E–03	3,1E–01 ± 9E–03	2,9E–02 ± 9E–04	5,6E–03 ± 2E–04	1,2E–03 ± 5E–05	
16°	7,7E–02 ± 1E–03	5,5E–02 ± 1E–03	1,7E–03 ± 4E–05	1,3E–04 ± 6E–06	1,5E–05 ± 2E–06	
40°	1,6E–02 ± 3E–04	2,0E–04 ± 8E–06				
60°	1,1E–03 ± 3E–05	3,0E–06 ± 6E–07				

Table 6. Production rates with statistical error in function of the charge of the fragments and the angle of detection for the 4 cm PMMA target. Values are in counts/(incident  $^{12}\text{C.sr}$ ).

PMMA thickness: 3 cm						
Angle	Nuclear charge					
	Z1	Z2	Z3	Z4	Z5	Z6
0°-BGO	2,4E–01 ± 7E–03	4,9E–01 ± 1E–02	1,4E–01 ± 4E–03	2,5E–02 ± 5E–04		
5°-BGO	2,2E–01 ± 5E–03	3,7E–01 ± 8E–03	6,3E–02 ± 1E–03	9,6E–03 ± 2E–04		
10°-BGO	1,5E–01 ± 5E–03	1,2E–01 ± 4E–03	4,2E–03 ± 2E–04	4,5E–04 ± 3E–05		
16°	4,8E–02 ± 8E–04	1,7E–02 ± 3E–04	1,2E–04 ± 4E–06	1,0E–05 ± 1E–06		
40°	8,0E–03 ± 1E–04	4,6E–05 ± 2E–06				
60°	4,2E–04 ± 1E–05	1,3E–06 ± 3E–07				

## Acknowledgment

We gratefully acknowledge the CHARISSA collaboration for providing us with the ECLAN reaction chamber.

## Appendix A

In Tables 1–6, results obtained with the telescope with the BGO scintillator are noted “angle°BGO”, the other results have been obtained with the CsI scintillator telescopes. The errors correspond to the statistical errors. The results obtained for  $Z = 1$  at forward angle with the “CsI telescopes” are slightly underestimated (20–50%). These results are highlighted in light grey in the tables.

## References

- [1] D. Schardt et al., Adv. Space Res. 17 (1996) 87–94.
- [2] M. Scholz, Nucl. Instrum. Methods B 76 (2000) 161–163.
- [3] O. Jäkel, M. Krämer, Physica Med. 14 (1) (1998) 53–62.
- [4] C.H. Tsao, R. Silberberg, A.F. Barghouty, L. Sihver, T. Kanai, Phys. Rev. C 47 (1993) 1257.
- [5] I. Gudowska, N. Sobolevsky, P. Andreo, D. Belkic, A. Brahme, Phys. Med. Biol. 49 (2005) 1933–1958.
- [6] I. Pshenichnov, I. Mishustin, W. Greiner, Phys. Med. Biol. 50 (2005) 5493–5507.
- [7] La Tessa, L. Sihver, C. Zeitlin, J. Miller, S. Guetersloh, L. Heilbronn, D. Mancusi, Y. Iwata, T. Murakami, Nucl. Phys. A 791 (2007) 434–450.
- [8] N. Matsufuji, A. Fukumura, M. Komori, T. Kanai, T. Kohno, Phys. Med. Biol. 48 (2003) 1605–1623.
- [9] N. Matsufuji, M. Komori, H. Sasaki, K. Akiu, M. Ogawa, A. Fukumura, E. Urakabe, T. Inaniwa, T. Nishio, T. Kohno, T. Kanai, Phys. Med. Biol. 50 (2005) 3393–3403.
- [10] A. Toshito et al., Phys. Rev. C 75 (2007) 054606.
- [11] I. Schall et al., Nucl. Instrum. Methods B 117 (1996) 221–234.
- [12] K. Gunzert-Marx, D. Schardt, R.S. Simon, Radiat. Prot. Dosim. 110 (2004) 595–600.
- [13] K. Gunzert-Marx, H. Iwase, D. Schardt, R.S. Simon, New J. Phys. 10 (2008) 075003.
- [14] I. Pshenichnov, A. Botvina, I. Mishustin, W. Greiner, Nucl. Instrum. Methods B 268 (2010) 604.
- [15] J.F. Ziegler, J.P. Biersack, U. Littmark, The Stopping and Range of Ions in Solids, vol. 1 The Stopping and Ranges of Ions in Matter, Pergamon Press, NY, (1985).
- [16] G. Farès et al., Eur. Phys. J. A 19 (2004) 105–116.
- [17] M. Golovkov, D. Aleksandrov, L. Chulkov, G. Kraus, D. Schardt, Adv. Hadrontherapy International Congress Series 1144 (1997) 316–324.
- [18] K. Ikeda, N. Takigawa, H. Horiuchi, Prog. Theor. Phys. Suppl. (1968) 464.
- [19] S. Agostini et al., Nucl. Instrum. Methods A 506 (2003) 205–303.
- [20] <http://www.fluka.org/fluka.php>.
- [21] E. Haettner, Experimental study on carbon ion fragmentation in water using GSI therapy beams, Master's Thesis Kungliga Tekniska Hogskolan Stockholm (2006).
- [22] E. Haettner, H. Iwase, D. Schardt, Radiat. Prot. Dosim. 122 (2006) 485–487.